Ring resonator-based on-chip modulation transformer for high-performance phase-modulated microwave photonic links

Leimeng Zhuang,[1,*] Caterina Taddei,[1] Marcel Hoekman,[2] Arne Leinse,[2] René Heideman,[2] Paulus van Dijk,[3] and Chris Roeloffzen[1, 3]

[1]Telecommunication Engineering group, University of Twente, PO Box 217, Enschede, 7500 AE, The Netherlands
[2]LioniX BV, PO Box 456, Enschede, 7500 AL, The Netherlands
[3]SATRAX BV, PO Box 456, Enschede, 7500 AL, The Netherlands
[*]l.zhuang@ewi.utwente.nl

Abstract: In this paper, we propose and experimentally demonstrate a novel wideband on-chip photonic modulation transformer for phase-modulated microwave photonic links. The proposed device is able to transform phase-modulated optical signals into intensity-modulated versions (or vice versa) with nearly zero conversion of laser phase noise to intensity noise. It is constructed using waveguide-based ring resonators, which features simple architecture, stable operation, and easy reconfigurability. Beyond the stand-alone functionality, the proposed device can also be integrated with other functional building blocks of photonic integrated circuits (PICs) to create on-chip complex microwave photonic signal processors. As an application example, a PIC consisting of two such modulation transformers and a notch filter has been designed and realized in TriPleX^{TM} waveguide technology. The realized device uses a 2×2 splitting circuit and 3 ring resonators with a free spectral range of 25 GHz, which are all equipped with continuous tuning elements. The device can perform phase-to-intensity modulation transform and carrier suppression simultaneously, which enables high-performance phase-modulated microwave photonics links (PM-MPLs). Associated with the bias-free and low-complexity advantages of the phase modulators, a single-fiber-span PM-MPL with a RF bandwidth of 12 GHz (3 dB-suppression band 6 to 18 GHz) has been demonstrated comprising the proposed PIC, where the achieved spurious-free dynamic range performance is comparable to that of Class-AB MPLs using low-biased Mach-Zehnder modulators.

©2013 Optical Society of America

OCIS codes: (130.3120) Integrated optics devices; (060.5625) Radio frequency photonics; (070.6020) Continuous optical signal processing; (060.2360) Fiber optic links and subsystems; (350.4010) Microwave.

References and links

1. J. Capmany and D. Novak, "Microwave photonics combines two worlds," Nat. Photonics **1**(6), 319–330 (2007).
2. J. Yao, "Microwave photonics," J. Lightwave Technol. **27**(3), 314–335 (2009).
3. D. A. I. Marpaung, C. G. H. Roeloffzen, R. G. Heideman, A. Leinse, S. Sales, and J. Capmany, "Integrated microwave photonics," Laser Photonics Rev., DOI:10.1002/Ipor.201200032, (2013).
4. A. Meijerink, C. G. H. Roeloffzen, R. Meijerink, L. Zhuang, D. A. I. Marpaung, M. J. Bentum, M. Burla, J. Verpoorte, P. Jorna, A. Hulzinga, and W. C. van Etten, "Novel ring resonator-based integrated photonic beamformer for broadband phased-array antennas-Part I: design and performance analysis," J. Lightwave Technol. **28**(1), 3–18 (2010).
5. L. Zhuang, C. G. H. Roeloffzen, A. Meijerink, M. Burla, D. A. I. Marpaung, A. Leinse, M. Hoekman, R. G. Heideman, and W. C. van Etten, "Novel ring resonator-based integrated photonic beamformer for broadband phased-array antennas-Part II: experimental prototype," J. Lightwave Technol. **28**(1), 19–31 (2010).
6. N. N. Feng, P. Dong, D. Feng, W. Qian, H. Liang, D. C. Lee, J. B. Luff, A. Agarwal, T. Banwell, R. Menendez, P. Toliver, T. K. Woodward, and M. Asghari, "Thermally-efficient reconfigurable narrowband RF-photonic filter," Opt. Express **18**(24), 24648–24653 (2010).

7. J. Lloret, J. Sancho, M. Pu, I. Gasulla, K. Yvind, S. Sales, and J. Capmany, "Tunable complex-valued multi-tap microwave photonic filter based on single silicon-on-insulator microring resonator," Opt. Express **19**(13), 12402–12407 (2011).

8. M. Ferrera, Y. Park, L. Razzari, B. E. Little, S. T. Chu, R. Morandotti, D. J. Moss, and J. Azaña, "On-chip CMOS-compatible all-optical integrator," Nat. Commun. **1**(29), doi:10.1038/ncomms1028 (2010).

9. F. Liu, T. Wang, L. Qiang, T. Ye, Z. Zhang, M. Qiu, and Y. Su, "Compact optical temporal differentiator based on silicon microring resonator," Opt. Express **16**(20), 15880–15886 (2008).

10. M. H. Khan, H. Shen, Y. Xuan, L. Zhao, S. Xiao, D. E. Leaird, A. M. Weiner, and M. Qi, "Ultrabroad-bandwidth arbitrary radiofrequency waveform generation with a silicon photonic chip-based spectral shaper," Nat. Photonics **4**(2), 117–122 (2010).

11. J. S. Fandiño, J. D. Doménech, P. Muñoz, and J. Capmany, "Integrated InP frequency discriminator for Phase-modulated microwave photonic links," Opt. Express **21**(3), 3726–3736 (2013).

12. D. A. I. Marpaung, C. G. H. Roeloffzen, A. Leinse, and M. Hoekman, "A photonic chip based frequency discriminator for a high performance microwave photonic link," Opt. Express **18**(26), 27359–27370 (2010).

13. K. Tan, D. A. I. Marpaung, R. Pant, F. Gao, E. Li, J. Wang, D. Y. Choi, S. Madden, B. Luther-Davies, J. Sun, and B. J. Eggleton, "Photonic-chip-based all-optical ultra-wideband pulse generation via XPM and birefringence in a chalcogenide waveguide," Opt. Express **21**(2), 2003–2011 (2013).

14. D. A. I. Marpaung, L. Chevalier, M. Burla, and C. G. H. Roeloffzen, "Impulse radio ultrawideband pulse shaper based on a programmable photonic chip frequency discriminator," Opt. Express **19**(25), 24838–24848 (2011).

15. L. Zhuang, W. P. Beeker, A. Leinse, R. G. Heideman, P. van Dijk, and C. Roeloffzen, "Novel wideband microwave polarization network using a fully-reconfigurable photonic waveguide interleaver with a two-ring resonator-assisted asymmetric Mach-Zehnder structure," Opt. Express **21**(3), 3114–3124 (2013).

16. L. Zhuang, M. R. Khan, W. P. Beeker, A. Leinse, R. G. Heideman, and C. G. H. Roeloffzen, "Novel microwave photonic fractional Hilbert transformer using a ring resonator-based optical all-pass filter," Opt. Express **20**(24), 26499–26510 (2012).

17. L. Zhuang, M. Hoekman, A. Leinse, R. G. Heideman, P. W. L. van Dijk, and C. G. H. Roeloffzen, "Novel low-loss waveguide delay line using Vernier ring resonators for on-chip multi-λ microwave photonic signal processors," Laser Photon. Rev. DOI 10.1002/lpor.201300053, (2013).

18. J. Sancho, J. Bourderionnet, J. Lloret, S. Combrié, I. Gasulla, S. Xavier, S. Sales, P. Colman, G. Lehoucq, D. Dolfi, J. Capmany, and A. De Rossi, "Integrable microwave filter based on a photonic crystal delay line," Nat. Commun. **3**(9), 1075 (2012).

19. M. Burla, D. A. I. Marpaung, L. Zhuang, C. G. H. Roeloffzen, M. R. Khan, A. Leinse, M. Hoekman, and R. G. Heideman, "On-chip CMOS compatible reconfigurable optical delay line with separate carrier tuning for microwave photonic signal processing," Opt. Express **19**(22), 21475–21484 (2011).

20. F. Morichetti, C. Ferrari, A. Canciamilla, and A. Melloni, "The first decade of coupled resonator optical waveguide: bringing slow light to applications," Laser Photon. Rev. **6**(1), 74–96 (2012).

21. A. Leinse, R. G. Heideman, M. Hoekman, F. Schreuder, F. Falke, C. G. H. Roeloffzen, L. Zhuang, M. Burla, D. A. I. Marpaung, D. H. Geuzebroek, R. Dekker, E. J. Klein, P. W. L. van Dijk, and R. M. Oldenbeuving, "TriPleX waveguide platform: low-loss technology over a wide wavelength range," In: Proceedings of SPIE Optics & Optoelectronics **8767,** (Proceedings of Integrated Photonics: Materials, Devices, and Applications II), 1–13 (2013).

22. L. Zhuang, D. A. I. Marpaung, M. Burla, W. P. Beeker, A. Leinse, and C. G. H. Roeloffzen, "Low-loss, high-index-contrast Si_3N_4/SiO_2 optical waveguides for optical delay lines in microwave photonics signal processing," Opt. Express **19**(23), 23162–23170 (2011).

23. W. Li, M. Li, and J. Yao, "A narrow-passband and frequency-tunable micro-wave photonic filter based on phase-modulation to intensity-modulation conversion using a phase shifted fiber bragg grating," IEEE Trans. Microw. Theory Tech. **60**(5), 1287–1296 (2012).

24. H. Chi, X. Zou, and J. Yao, "Analytical models for phase-modulation-based microwave photonic systems with phase modualtion to intensity modulation conversion using a dispersive device," J. Lightwave Technol. **27**(5), 511–521 (2009).

25. A. Perentos, F. Cuesta-Soto, A. Canciamilla, B. Vidal, L. Pierno, N. S. Losilla, F. Lopez-Royo, A. Melloni, and S. Iezekiel, "Using a Si_3N_4 ring resonator notch filter for optical carrier reduction and modulation depth enhancement in radio-over-fiber links," IEEE Photon. J. **5**(1), 00110 (2013).

26. L. Liu, S. Zheng, X. Zhang, X. Jin, and H. Chi, "Performances improvement in radio over fiber link through carrier suppression using stimulated brillouin scattering," Opt. Express **18**(11), 11827–11837 (2010).

27. V. J. Urick, F. Bucholtz, P. S. Devgan, J. D. Mckinney, and K. J. Williams, "Phase modualtion with interferometric detection as an alternative to intensity modulation with direct detection for analog-photonic links," IEEE trans. MTT **55**(9), 1978–1985 (2007).

28. M. J. LaGasse and S. Thaniyavarn, "Bias-free high-dynamic-range phase-modulated fiber-optic link," IEEE Photon. Technol. Lett. **9**(5), 681–683 (1997).

29. T. Darcie and P. Driessen, "Class-AB techniques for high-dynamic-range microwave-photonic links," IEEE Photon. Technol. Lett. **18**(8), 929–931 (2006).

30. J. Bull, T. Darcie, J. Zhang, H. Kato, and N. Jaeger, "Broadband class-AB microwave-photonic link using polarization modulation," IEEE Photon. Technol. Lett. **18**(9), 1073–1075 (2006).

31. C. H. Cox III, *Analog Optical Links* (Cambridge, 2004).

32. C. K. Madsen and J. H. Zhao, *Optical Filter Design and Analysis* (Wiley, 1999).

33. L. Nichols, K. Williams, and R. Estman, "Optimizing the ultrawide-band photonic link," IEEE Trans. Microw. Theory Tech. **45**(8), 1384–1389 (1997).
34. E. Ackerman, S. Wanuga, J. MacDonald, and J. Prince, "Balanced receiver external modulation fiber-optic link architecture with reduced noise figure," in Proc. IEEE MTT-S Int. Microwave Symp. **2**, 723–726 (1993).

1. Introduction

Microwave/RF signal processing based on integrated microwave photonic (MWP) signal processors has been evolving with remarkable pace in the past decade [1–3]. Beside the common advantages of optical devices such as large instantaneous bandwidth, low loss and power consumption, small size and weight, effective reduction on electromagnetic interference, and system reconfigurability, the on-chip integration approach also features high robustness and compactness, and large potentials of significant system cost reduction. This superiority not only means that on-chip MWP signal processors have strong potentials for large-scale proliferation and industrialization, but also promises that they will grow fast into a strong market competitor for conventional microwave/RF electronics in the near future. Driven by this goal, numerous on-chip MWP functionalities have been studied and demonstrated in the recent years, where several salient works include photonic beamformer [4, 5], spectrum filter [6, 7], integrator [8], differentiator [9], arbitrary waveform generator [10], frequency discriminator [11, 12], UWB pulse shaper [13, 14], fractional Hilbert transformer [15, 16], and tunable delay line [17–20].

Notably, most of those realized on-chip MWP functionalities incorporate the use of ring resonators, a key and versatile device for integrated MWP signal processors. In this paper, we present a novel ring resonator-based device, which is able to transform phase-modulated (PM) optical signals into the intensity-modulated (IM) versions (or vice versa) with nearly zero conversion of laser phase noise to intensity noise. This so-called modulation transformer features simple architecture, stable operation, and easy reconfigurability. Beyond the stand-alone functionality, the proposed device can also be integrated with other functional building blocks of photonic integrated circuits (PICs) to create on-chip complex microwave photonic signal processors. As an application example, a PIC consisting of two such modulator transformers and a notch filter has been designed and realized in low-loss, high-index-contrast TriPleX^{TM} waveguide technology [21, 22]. The realized device uses a 2×2 splitting circuit and 3 ring resonators with a free spectral range of 25 GHz, which are all equipped with continuous tuning elements. The device can perform phase-to-intensity modulation transform [23, 24] and carrier suppression [25, 26] simultaneously, which enables high-performance phase-modulated microwave photonics links (PM-MPLs) [11, 12, 27, 28]. Associated with the bias-free and low-complexity advantages of the phase modulators, a single-fiber-span PM-MPL with a RF bandwidth of 12 GHz (3 dB-suppression band 6 to 18 GHz) has been demonstrated comprising the proposed PIC, where the achieved spurious-free dynamic range performance is comparable to that of Class-AB MPLs using low-biased Mach-Zehnder modulators (MZMs) [29, 30].

This paper is organized as follows. Section II describes the device and system principles. Section III copes with the device design and realization. The characterization of the realized PIC and its application for PM-MPLs are presented in Section IV. The conclusions and discussions are formulated at the end of the paper.

2. Device and system principles

2.1 PM-to-IM transform

The MZM-based intensity modulation and phase modulation are both inherent to the linear optical phase variation induced by the amplitude variation of modulation electrical signals [31]. The complex amplitudes of the quadrature-biased IM and PM signals can be expressed in similar forms [24, 26], where the frequency-component breakdowns can be given by

$$E_{\text{MZM-Q}}(t) = E_{\text{in}}\sqrt{L}\cos(\frac{\pi}{4} + m_{\text{MZM}}\cos(2\pi f_{\text{RF}}t + \phi_{\text{RF}}))$$

$$= E_{\text{in}}\sqrt{L/2}[\cos(m_{\text{MZM}}\cos(2\pi f_{\text{RF}}t + \phi_{\text{RF}})) - \sin(m_{\text{MZM}}\cos(2\pi f_{\text{RF}}t + \phi_{\text{RF}}))]$$

$$= E_{\text{in}}\sqrt{L/2}[\sum_{k=-\infty}^{\infty}\exp(j\frac{\pi}{2}2k)J_{2k}(m_{\text{MZM}})\exp(j2k(2\pi f_{\text{RF}}t + \phi_{\text{RF}}))$$

$$+ j\sum_{k=-\infty}^{\infty}\exp(j\frac{\pi}{2}(2k+1))J_{2k+1}(m_{\text{MZM}})\exp(j(2k+1)(2\pi f_{\text{RF}}t + \phi_{\text{RF}}))]$$

(1)

$$E_{\text{PM}}(t) = E_{\text{in}}\sqrt{L}\exp(jm_{\text{PM}}\cos(2\pi f_{RF}t + \phi_{\text{RF}}))$$

$$= E_{\text{in}}\sqrt{L}\sum_{k=-\infty}^{\infty}j^{k}J_{k}(m_{\text{PM}})\exp(jk(2\pi f_{RF}t + \phi_{\text{RF}}))$$

(2)

where E_{in} is the amplitude of the input CW light, L is the optical loss of the modulator, J_n is the nth-order Bessel function of the first kind, m denotes the modulation index which is related to the RF signal amplitude A_{RF} and modulator RF halfwave voltage V_{π} by $m_{\text{MZM}} = A_{\text{RF}}/2V_{\pi\text{-MZM}}$ and $m_{\text{PM}} = A_{\text{RF}}/V_{\pi\text{-PM}}$. Since the phase of the modulation signal ϕ_{RF} does not have impact on the amplitude of the modulated signals, we assume $\phi_{\text{RF}} = \pi$ for Eq. (1) and $\phi_{\text{RF}} = \pi/2$ for Eq. (2) for the sake of easy comparison. Then, using a small signal assumption where the 3rd- and higher-order modulation sidebands are negligible, Eq. (1) and Eq. (2) can be respectively reduced to

$$E_{\text{MZM-Q}}(t) = \eta_{\text{MZM}}[J_0(m_{\text{MZM}}) + J_1(m_{\text{MZM}})\exp(j2\pi f_{\text{RF}}t) - J_{-1}(m_{\text{MZM}})\exp(-j2\pi f_{\text{RF}}t)$$

$$-J_2(m_{\text{MZM}})\exp(j2\pi 2f_{\text{RF}}t) - J_{-2}(m_{\text{MZM}})\exp(-j2\pi 2f_{\text{RF}}t)]$$

(3)

$$E_{\text{PM}}(t) = \eta_{\text{PM}}[J_0(m_{\text{PM}}) - J_1(m_{\text{PM}})\exp(j2\pi f_{\text{RF}}t) - J_{-1}(m_{\text{PM}})\exp(-j2\pi f_{\text{RF}}t)$$

$$+J_2(m_{\text{PM}})\exp(j2\pi 2f_{\text{RF}}t) + J_{-2}(m_{\text{PM}})\exp(-j2\pi 2f_{\text{RF}}t)]$$

(4)

where $\eta_{\text{MZM}} = E_{\text{in}}\sqrt{L/2}$ and $\eta_{\text{PM}} = E_{\text{in}}\sqrt{L}$. Comparing Eq. (3) and Eq. (4), it is straightforward to see that the two modulation types are in nature only different in the signs of their sidebands relative to the carrier. For example, the IM signal in Eq. (3) has $+ J_1$ for the 1st-order upper sideband, while the PM signal in Eq. (4) has $-J_1$. This means that the PM can be transformed to IM (or vice versa) if the signs of the sidebands relative to the carrier can be manipulated. In principle, this manipulation can be implemented using an optical filter which features a unity magnitude response and a phase response as illustrated in Fig. 1. Moreover, it is also shown in Fig. 1 that the RF phase of the transformed signal can be manipulated to two anti-phase statuses by frequency-aligning the filter phase response to the optical signal spectrum differently (see Case 1 and Case 2 for instance).
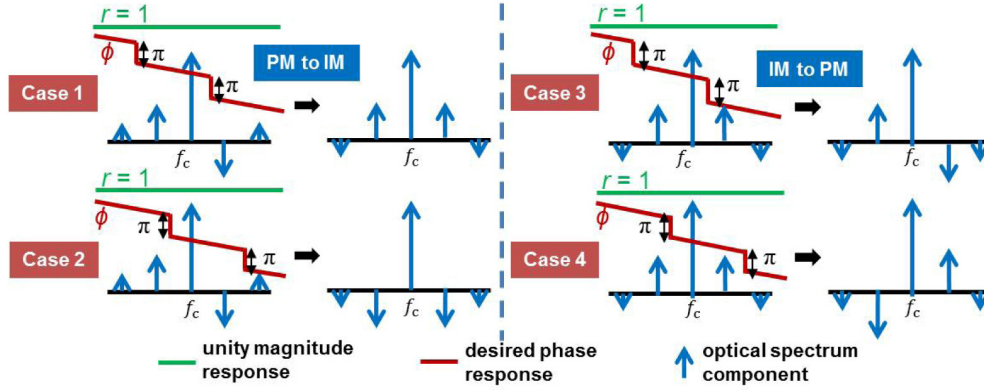
Fig. 1. Phase-domain illustration of modulation transform between PM and IM by means of sideband phase manipulation.

2.2 Frequency responses of one-coupler ring resonators

To implement the desired filter response in Fig. 1, one interesting way is to use one-coupler ring resonators (RRs). A schematic of a waveguide-based RR is depicted in the inset of Fig. 2(a), which is constructed using a 2×2 power coupler with one arm incorporated in a closed loop. The transfer function and the derived frequency responses of a RR, namely power and phase responses, can be respectively expressed by

$$H_{\mathrm{RR}}(v) = \frac{\sqrt{1-\kappa} - \sqrt{r}e^{-j(v+\theta)}}{1 - \sqrt{r(1-\kappa)}e^{-j(v+\theta)}} \tag{5}$$

$$\left| H_{\mathrm{RR}}(v) \right|^2 = \frac{1 - \kappa + r - 2\sqrt{r(1-\kappa)}\cos(v+\theta)}{1 + r\sqrt{1-\kappa} - 2\sqrt{r(1-\kappa)}\cos(v+\theta)} \tag{6}$$

$$\Psi_{\mathrm{RR}}(v) = \arctan\left[\frac{\sqrt{r}\sin(v+\theta)}{\sqrt{1-\kappa} - \sqrt{r}\cos(v+\theta)}\right] - \arctan\left[\frac{\sqrt{r(1-\kappa)}\sin(v+\theta)}{1 - \sqrt{r(1-\kappa)}\cos(v+\theta)}\right] \tag{7}$$

where $v = 2\pi f/\Delta f_{\mathrm{FSR}}$ is the angular frequency normalized to the free spectral range (FSR), Δf_{FSR}, of the RR, κ is the power coupler coupling coefficient, θ represents an additional roundtrip optical phase shift of the ring loop, and r is the roundtrip power transmission coefficient. In practice, κ and θ can be implemented as tuning elements, where κ determines the shape of the frequency responses, and θ controls the response frequency shift [22]. Ideally, a lossless RR ($r = 1$) is a 1st-order all-pass filter characterized by a unity magnitude response [32]. However, the waveguide propagation loss induces power transmission notches at the resonance frequencies of the RR. This device property is depicted in Fig. 2(a), where the notch depth can be varied by changing κ. In Fig. 2(b), the phase responses of the RR for different κ are depicted. Evidently, the desired phase jump of π as shown in Fig. 1 can be approximated by setting κ to 0.87 [16]. Moreover, it is demonstrated in Fig. 2(c) that the frequency shift of the RR responses can be achieved by varying θ. For simplicity, we assume that the optical signal has its carrier aligned to a resonance frequency of the RR with the status $\theta = 0$. Then, using the tuning properties of the device, two phase response configurations which implement Case 1 and Case2 of Fig. 1 can be achieved. An illustration of this is shown in Fig. 2(d). Compared to the ideal abrupt π-phase jumps in the desired phase responses, the RR introduces phase errors due to the intrinsic phase transition shape of the device. Consequently, this will have impact on the 3 dB-suppression bandwidth of the device. A further discussion on bandwidth is given in Section 2.4.
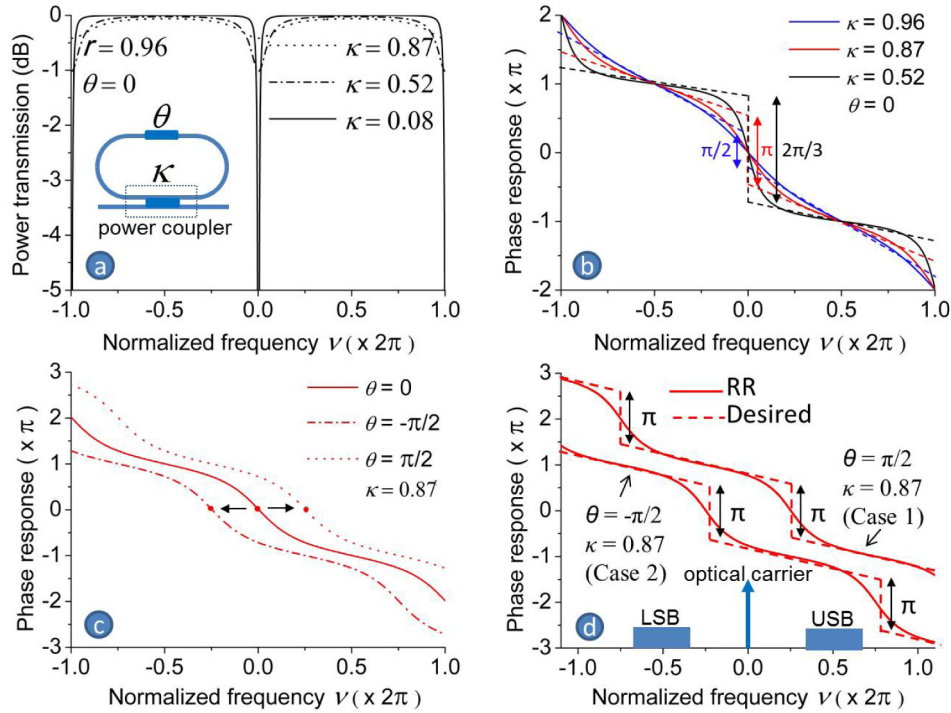
Fig. 2. (a) a schematic of a RR and the simulated power transmissions; (b) simulated phase responses of the RR and the corresponding phase-jump approximations; (c) a demonstration of frequency shift by varing θ; (d) an illustration of two phase response configurations to implement Case 1 and Case 2 of Fig. 1.

2.3 System architecture for PM-MPLs

As an application example, the proposed modulation transformer is used to enable a PM-MPL. The simplest system architecture is depicted in Fig. 3(a), where the RR performs the modulation transformer functionality as in either Case 1 or Case 2 in Fig. 1. For this system architecture, it is straightforward to understand that the detector output contains not only the desired RF signal but also the baseband and higher-order components as distortions, resulting from the nonlinear natures of the phase modulation and the square-law property of photodiodes [4]. To improve the system performance, the architecture depicted in Fig. 3(b) can be used, which incorporates a more advanced design of PIC and a balanced photodetector. In the PIC, a 3-dB coupler split the optical signal into two equal portions, which are sent through two individual RRs in a parallel manner. As indicated in Fig. 3(b), the upper RR and lower RR are used to perform the modulation transforms of Case 1 and Case 2 in Fig. 1, respectively. Consequently, two versions of IM signals with opposite RF phases are produced at the two outputs of the PIC, which facilitate the balanced photodetector to cancel out the DC and even-order components in its output [4]. Note that the output signal pair of the PIC conforms to that of a dual-output MZM [33, 34]. Therefore, the well-known MZM-based MPL performance facts also apply to this case. Furthermore, owing to the use of the same PIC building blocks, a RR-based reconfigurable notch filter can be added before the 3-dB coupler to create a system architecture as shown in Fig. 3(c), which we propose as a novel implementation of a PM-MPL. The added notch filter can be used to perform the carrier suppression technique, which allows an extra link gain of $1/\chi$ given a constant average photocurrent I_{DC} (per photodiode) and χ indicates the carrier suppression ratio determined by the notch depth [25, 26]. In fact, this system architecture renders the proposed PM-MPL an analogy to a Class-AB MPL using a pair of low-biased MZMs [29, 30].
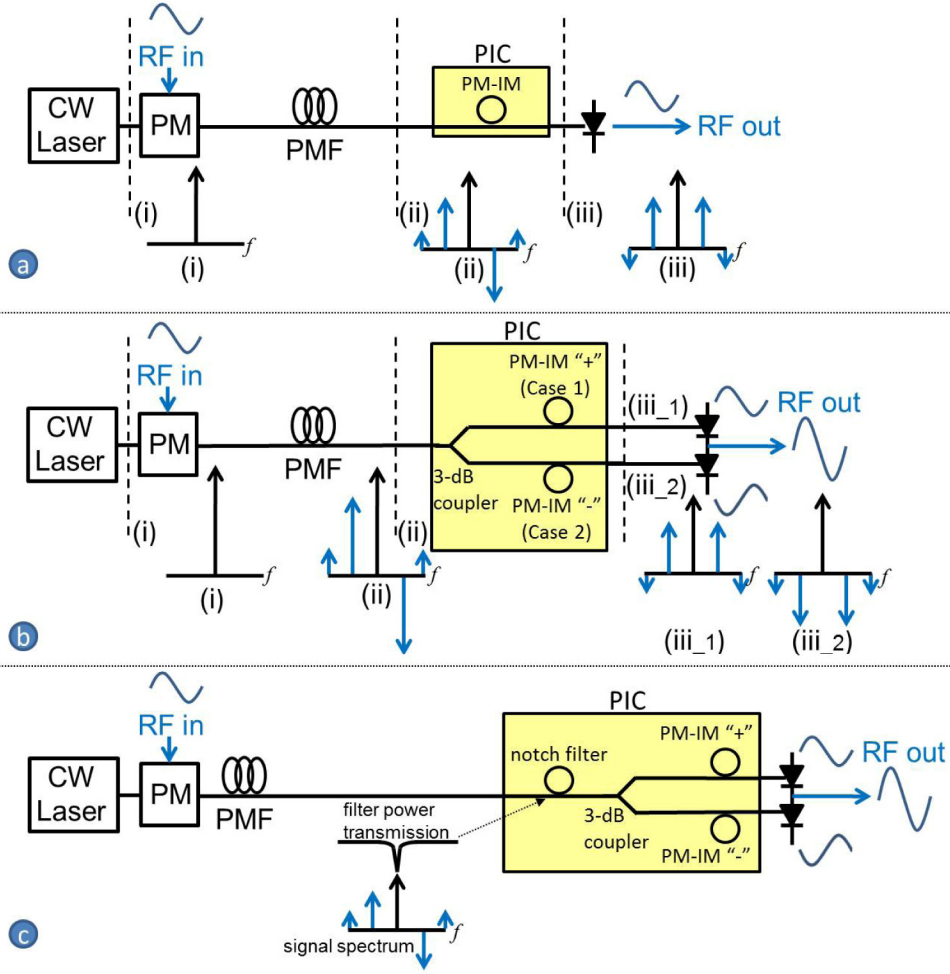
Fig. 3. (a-c) system architectures and the phase-domain signal spectrum schematics of the proposed PM-MPL using RR-based modulation transformers and notch filter.

2.4 Link performance analysis

2.4.1 Bandwidth

Assuming that the RF bandwidth of the PM-MPL is dictated by the proposed modulation transformer (the remainder optical and electrical components have infinite bandwidth), then using the system principle and optical transfer function of the RR in Eq. (5), the equivalent RF transfer function of the RR-based modulation transformer (MT) can be calculated by

$$
\begin{aligned}
H_{RF}(\nu_{RF}) &= \Gamma_U + \Gamma_L \\
&= \frac{1}{2}[H_{RR}^{MT}(-\Delta\nu)^* H_{RR}^{MT}(\nu_{RF} - \Delta\nu)] + \frac{1}{2}[-H_{RR}^{MT}(-\nu_{RF} - \Delta\nu)^* H_{RR}^{MT}(-\Delta\nu)]
\end{aligned} \tag{8}
$$

where Γ_U and Γ_L indicate the beat product contributions from the upper and lower optical sidebands, respectively, $\nu_{RF} = 2\pi\Delta f_{RF}/\Delta f_{FSR}$ is the normalized RF frequency, and $\Delta\nu = 2\pi\Delta f/\Delta f_{FSR} = |\theta|$ denotes the normalized frequency spacing between RR resonance and the optical carrier (for example, $\Delta\nu = |\theta| = \pi/2$ in Fig. 2(b)). Figure 4(a) depicts the shape of the RF power transmission $|H_{RF}|^2$ in a RF frequency range equal to the FSR of the RR. The

resulting 3 dB-suppression bandwidths and the maximum RF passband transmissions for different values of Δv are depicted in Fig. 4(b). In these simulations, the RR frequency responses for $\kappa = 0.87$ are considered as depicted in Fig. 2. To give a numerical example, when $\Delta v = 0.4\pi$ and $r = 0.96$ (-0.17 dB), the resulting 3-dB bandwidth and maximum RF transmission are $0.5\Delta f_{\mathrm{FSR}}$ and -0.5 dB, respectively, as shown in Fig. 4(b).
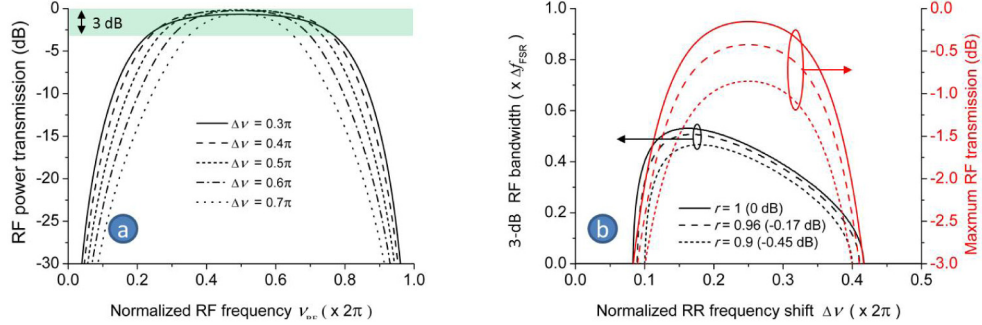

Fig. 4. (a) simulated equivalent RF power transmissions of the RR-based modulation transformer for different values of Δv, where $\kappa = 0.87$ and $r = 1$ are considered, (b) the 3-dB RF bandwidth and maximum passband transmission versus Δv.

2.4.2 Gain and noise

As mentioned in Section 2.3, the proposed PM-MPL performs as an analogy of a Class-AB MPL using a pair of low-biased MZMs. Therefore, similar gain and noise expressions can be used [27–30], which are given in Table 1. Moreover, unlike the PM-MPLs using frequency discriminators [12], the proposed PM-MPL can operate with nearly zero conversion of the laser phase noise to intensity noise. This feature can be achieved by means of setting Δv such that the RR-based modulation transformers have nearly zero slope of the power transmission at the optical carrier frequency, or in other words, the optical carrier should be positioned in the "flat-band" in Fig. 2(a). An experimental verification of this is given in Section 4.2.

2.4.3 Nonlinearity

In principle, the proposed PM-MPL is free of even-order intermodulation distortions (IMDs), owing to the system scheme using a balanced photodetector [4]. For the 3rd-order IMD, the spur in the RF output is generated from the same mechanism as for MZM-MPLs. However, in this case, the RRs in the optical paths will introduce an additional modification to the optical signal spectrum, which will lead to changes in the system linearity performance. To determine these changes, the following derivations can be used. Suppose two-tone transmission with RF frequencies f_{RF1} and f_{RF2} ($f_{\mathrm{RF2}} > f_{\mathrm{RF1}}$), then the complex signal amplitude after serially passing through the notch filter (NOF) and a modulator transformer (MT) as depicted in Fig. 3(c) can be expressed by

$$
\begin{aligned}
E_{\mathrm{out}}(t) \\
= E_{\mathrm{in}} \frac{\sqrt{2L}}{2} \exp[-\mathrm{j}m_{\mathrm{RF1}}\cos(2\pi f_{\mathrm{RF1}}t) - \mathrm{j}m_{\mathrm{RF2}}\cos(2\pi f_{\mathrm{RF2}}t + \varphi)] \otimes h_{\mathrm{RR}}^{\mathrm{NOF}}(t) \otimes h_{\mathrm{RR}}^{\mathrm{MT}}(t) \\
= E_{\mathrm{in}} \frac{\sqrt{2L}}{2} \sum_{p=-\infty}^{\infty}\sum_{q=-\infty}^{\infty} \mathrm{j}^{p+q} J_p(m_{\mathrm{RF1}}) J_q(m_{\mathrm{RF2}}) \exp[\mathrm{j}2\pi(pf_{\mathrm{RF1}} + qf_{\mathrm{RF2}})t \quad (9) \\
+ \mathrm{j}q\varphi] H_{\mathrm{RR}}^{\mathrm{NOF}}(v_{p,q}) H_{\mathrm{RR}}^{\mathrm{MT}}(v_{p,q} - \Delta v) \\
= E_{\mathrm{in}} \frac{\sqrt{2L}}{2} \sum_{p,q} \Gamma_{p,q}
\end{aligned}
$$

where φ is an initial phase difference between the two RF tones, and $v_{p,q} = 2\pi(pf_{RF1} + qf_{RF2})/\Delta f_{FSR}$ is the normalized RF frequency. The beating between any two optical components in Eq. (9) leads to the generation of different orders of electrical harmonics and IMD products [24], where a photocurrent component with a frequency of $n_1f_{RF1} + n_2f_{RF2}$ can be expressed by

$$I_{n_1,n_2}(t) = r_{PD}\frac{|E_{in}|^2 L}{2}\mathrm{Re}\{\sum_{p,q}\Gamma_{p+n_1,q+n_2}\Gamma^*_{p,q}\} = A\cdot\mathrm{Re}\{\sum_{p,q}\Gamma_{p+n_1,q+n_2}\Gamma^*_{p,q}\} \qquad (10)$$

where r_{PD} denotes the responsivity of the detector and $\mathrm{Re}\{.\}$ indicates the real part of the complex signal. For the sake of simplicity, we assume that $m_{RF1} = m_{RF2} = m$ and a small signal approximation is applicable where only $\Gamma_{p,q}$'s with frequencies $\leq 2f_{RF2}$ are considered for contributions in Eq. (10). Then, the amplitudes of the RF fundamental and IMD3 components can be described as functions of the modulation index m, where the 3rd-order input interception point (IIP3) of the proposed PM-MPL can be determined (derivations are given in Appendix). Then, by comparing the resulting IIP3$_{PM-RR}$ to that of an MZM-MPL with the same modulation index IIP3$_{MZM}$, the impact of the RRs (the notch filter and the modulation transformer) on the system linearity can be quantified. For calculation easiness, we define this impact as relative IIP3 (RIP3), namely RIP3$_{PM-RR}$ = IIP3$_{PM-RR}$/IIP3$_{MZM}$ or (RIP3$_{PM-RR}$)$_{dB}$ = (IIP3$_{PM-RR}$)$_{dBm}$ − (IIP3$_{MZM}$)$_{dBm}$. An example of RIP3$_{PM-RR}$ calculation is depicted in Fig. 5, where device parameters $\kappa = 0.87$, $r = 0.96$, and $\Delta v = 0.4\pi$ are considered.
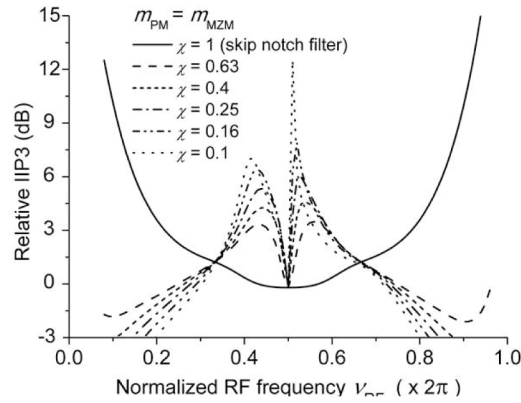

Fig. 5. Calculated RIP3$_{PM-RR}$ as a function of the normalized RF frequency, where device parameters $\kappa = 0.87$, $r = 0.96$, and $\Delta v = 0.4\pi$ are considered.

2.4.4 Spurious-free dynamic range (SFDR)

The proposed PM-MPL should have an infinite IMD2-SFDR because of the even-order cancellation of the balanced photodetector. For the IMD3-SFDR, a comparison between the proposed PM-MPL and MZM-MPLs is shown in Table 1. Evidently, under the condition of equal average photocurrent I_{DC}, the PM-to-IM approach using ideal modulation transformer responses will provide the same IMD3-SFDR as an MPL using quadrature-biased dual-output MZM. However, a SFDR improvement can be achieved by means of the carrier suppression technique implemented using a notch filter, which is analogous to the approach with low-biased MZMs. To give a numerical example, suppose that the proposed PM-MPL operates with $f_{RF} = 10$ GHz, $\Delta f_{FSR-RR} = 25$ GHz, $\Delta v = 0.4\pi$, $\chi = 0.1$, $r = 0.96$, $I_{DC} = 12$ mA, and $R_L = 50$ Ω, then one can calculate $|H_{RF}(f_{RF})|^2 = -0.5$ dB, RIP3$_{PM-RR} = 3$ dB, and IMD3-SFDR = 2/3[OIP3$_{dBm}$−(S_{shot}/4)$_{dBm/Hz}$] = 2/3[27.1 dBm−(−163.2 dBm/Hz)] = 126.9 dB.Hz$^{2/3}$ for the shot noise-limited scenario.

Table 1. Link performance metrics

Link type	DO MZM (Q-biased)	Class-AB MZM (Low-biased)	PM-to-IM (Ideal MT)	PM-to-IM (RR)
I_{DC} per photodiode	$\dfrac{r_{PD}P_{in}}{2L}$	$\dfrac{r_{PD}P_{in}}{4L}(1-\cos\phi_b)$	$\dfrac{r_{PD}P_{in}\chi}{2L}$	$\dfrac{r_{PD}P_{in}\chi}{2L}$
Link gain	$\left(\dfrac{\pi R_L I_{DC}}{V_{\pi\_MZM}}\right)^2$	$\left[\dfrac{\pi R_L I_{DC}\sin\phi_b}{V_{\pi\_MZM}(1-\cos\phi_b)}\right]^2$	$\dfrac{1}{\chi}\left(\dfrac{2\pi R_L I_{DC}}{V_{\pi\_PM}}\right)^2$	$\left[\dfrac{1}{\chi}\left(\dfrac{2\pi R_L I_{DC}}{V_{\pi\_PM}}\right)^2\right]H_{RF}^2$
IIP3	$\dfrac{4}{R_L}\left(\dfrac{V_{\pi\_MZM}}{\pi}\right)^2$	$\dfrac{4}{R_L}\left(\dfrac{V_{\pi\_MZM}}{\pi}\right)^2$	$\dfrac{4}{R_L}\left(\dfrac{V_{\pi\_PM}}{2\pi}\right)^2$	$\dfrac{4}{R_L}\left(\dfrac{V_{\pi\_PM}}{2\pi}\right)^2 RIP3_{PM\text{-}RR}$
OIP3	$4I_{DC}^2 R_L$	$4\left(\dfrac{I_{DC}\sin\phi_B}{1-\cos\phi_B}\right)^2 R_L$	$\dfrac{4}{\chi}I_{DC}^2 R_L$	$\dfrac{4}{\chi}I_{DC}^2 R_L H_{RF}^2 RIP3_{PM\text{-}RR}$

Link output noise power spectrum density

$S_{noise} = S_{th} + 1/4(S_{shot} + S_{RIN})$ (impedance-matched case)

$S_{th} = (1 + G_{link})k_B T$

$S_{shot} = 2qI_{DC}R_L$

$S_{RIN} = RINsys(I_{DC})^2 R_L$

IMD3-SFDR

$SFDR = 2/3(OIP3_{dBm} - S_{noise\_dBm/Hz}) = 2/3(IIP3_{dBm} + G_{link\_dBm} - S_{noise\_dBm/Hz})$

Suppose constant I_{DC} for all link type, then

$$SFDR_{MZM\_AB} = SFDR_{MZM\_DO} + \frac{2}{3}\left[\left(\frac{\sin\phi_B}{1-\cos\phi_B}\right)^2\right]_{dB}$$

$$SFDR_{PM\_ID} = SFDR_{MZM\_DO} + \frac{2}{3}\left[\frac{1}{\chi}\right]_{dB}$$

$$SFDR_{PM\_RR} = SFDR_{MZM\_DO} + \frac{2}{3}\left[\frac{H_{RR}^2 RIP3_{PM\text{-}RR}}{\chi}\right]_{dB}$$

P_{in}: optical power at modulator input	k_B: boltzmann constant,
R_L: load resistance	q: electron charge
ϕ_B: bias angle ($\phi_{B,Q} = \pi/2$)	RIN_{sys}: relative intensity noise of the system

3. Device realization

For the purpose of proof-of-concept, a PIC consisting of a 2 × 2 coupler and 3 RRs of a FSR of 25 GHz is used, which is a part of a complex MWP signal processor chip realized in TriPleX^{TM} waveguide technology, a proprietary technology of LioniX B.V [21, 22]. The device footprint measures approximately 8 mm × 1 mm. Figure 6 depicts the device mask layout, where the standard TriPleX^{TM} building blocks are used [17]. In this device, the couplers are implemented using Mach-Zechder interferometers, and the tunability of the device parameters (κ's and θ's) is realized by means of the thermo-optical effect of the waveguide, for which resistor-based heaters are placed on top of the designated waveguide sections. To achieve the full tuning ranges of $\kappa = [0, 1]$ and $\theta = [0, 2\pi]$, heater driving powers of 0.3 W and 0.6 W are required, respectively. These heaters allow for a tuning speed of 2 KHz. Their temperature changing range during operation is on the negligible level regarding its impact on the waveguide propagation loss which measures to be 0.2 dB/cm in this device.

For the full operation of the designed functionalities, the chip is fiber-pigtailed and mounted on a custom-designed printed circuit board, where the electrical connections to the chip are established by means of wire bonding. Moreover, the chip temperature stabilization is implemented using a peltier element-based cooling system attached to the bottom side of the chip. For the simultaneous control of multiple heaters, a computer-monitored 12-bit multi-channel voltage supplier is used, a dedicated control system developed by SATRAX B.V..
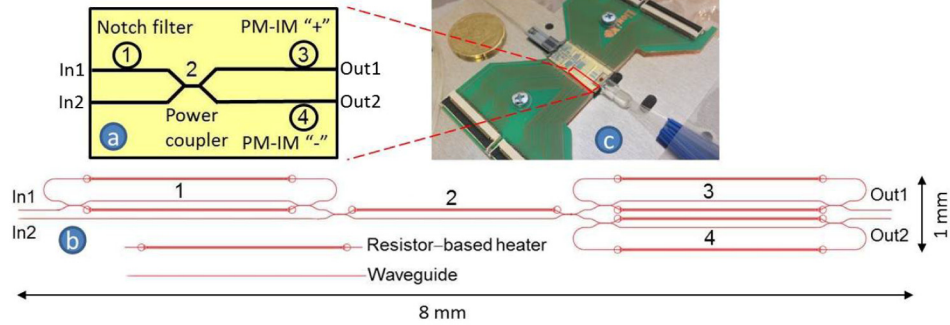
Fig. 6. (a) schematic and (b) mask layout of the proposed modulation transformer PIC, which is part of a complex MWP signal processor chip realizaed in TriPleX^{TM} waveguide technology; (c) a photo of the packaged chip with full optical and electrical connections.

4. Experimental verification

4.1 Measurement setup

The experimental setups depicted in Fig. 7(a) and Fig. 7(b) were established to characterize the PIC and the link performance, respectively. The used major components and equipment include a CW laser (EM4-253-80-057) driven by a low-noise current controller (ILX Lightwave LDX-3620), a Mach-Zehnder intensity modulator (Avanex PowerLog FA-20), a phase modulator (EO space PM-5K5-10), a RF balanced detector (Discovery semiconductor DSC710), two RF generators (Agilent PSG Vector signal generator E8267D), a RF vector network analyzer (Agilent NA5230A PNA-L), and a RF spectrum analyzer (Agilent N9020A MXA Signal Analyzer).
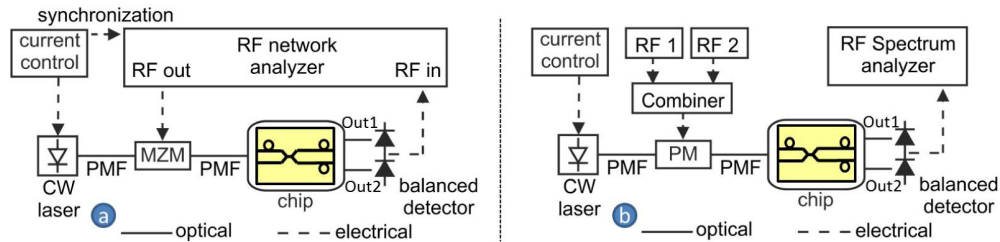

Fig. 7. (a) measurement setup for the characterizations of the PIC, (b) measurement setup for the characterization of link performance.

4.2 Measurement results

4.2.1 RR frequency responses

To achieve the desired frequency responses of the RRs, the measurement setup in Fig. 7(a) was used, where the phase-shift method is applied to determine the optical magnitude and phase responses from electrical S_{21} measurements [22]. In our case, an optical carrier modulated by a 50 MHz RF signal is frequency-swept through a full FSR of the device. In order to measure each RR independently, the device was reconfigured such that only one target RR is in operation between the input and output, while the other RRs are either

bypassed or decoupled from the bus waveguide (by means of setting $\kappa = 0$, namely zero portion of the light is coupled between the bus waveguide and the RR). Then, the S_{21} measurements based on the detected RF signal can be mathematically converted to their optical versions, since RF power transmission varies quadratically to the optical one, and RF phase shift varies linearly to the optical group delay which is the 1st-order derivative of the optical phase shift [22]. With respect to the device FSR of 25 GHz, a RF frequency of 50 MHz was chosen in order to achieve satisfying measurement resolution and accuracy simultaneously. Figure 8 depicts the measurement results, where the achieved RR frequency responses for the modulation transformer functionality is presented in Fig. 8(a), and the relative positions of the resonance frequencies (transmission dips or group delay peaks) of the three RRs are demonstrated in Fig. 8(b).
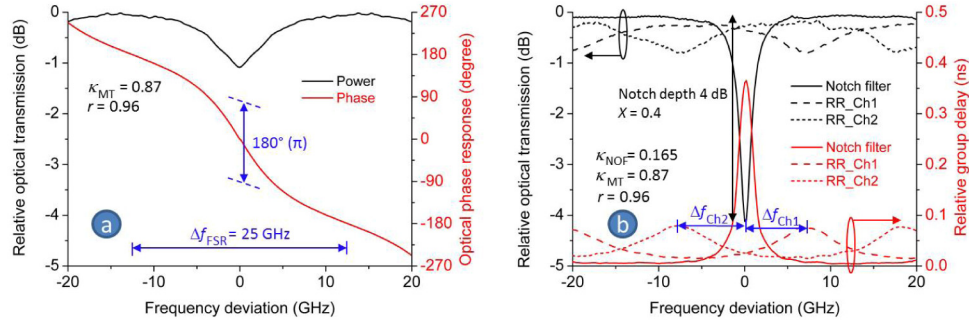
Fig. 8. (a) frequency response of the RRs optimized for the modulation transformer functionality, (b) demonstration of the relative positions of the resonance frequencies (transmission dips or group delay peaks) of the three RRs in the PIC.

4.2.2 Device RF functionalities

Using the RR frequency responses as shown in Fig. 8, a CW optical carrier with phase modulation of a RF frequency sweeping from 10 MHz to 20 GHz was sent through the PIC, where the optical carrier frequency is aligned to the notch point and the two RR-based modulation transformers are frequency-shifted such that the frequency spacing between the RR resonances and the optical carrier satisfies $\Delta f_{Ch1} = \Delta f_{Ch2} = \Delta f$ as shown in Fig. 8(b). Then, by performing S_{21} measurements, the device RF functionalities and bandwidth were verified. In order to accurately characterize the PIC, a system calibration was first performed, which eliminates the effects of the other optical and RF components in the measurement results. Figure 9(a) verifies the system principle of the proposed PM-MPL by showing the detected RF signals at the balanced photodetector output. Figure 9(b) demonstrates the RF bandwidth dependency on Δf in comparison to the simulations, where a RF bandwidth of 12 GHz (3 dB-suppression band 6 to 18 GHz) was measured for $\Delta f = 5$ GHz ($\Delta v = 0.4\pi$). Moreover, the extra gain introduced by performing the carrier suppression technique is demonstrated in Fig. 9(c), where a constant average photocurrent I_{DC} are maintained for the two measurements by means of a tunable optical attenuator inserted before the phase modulator.
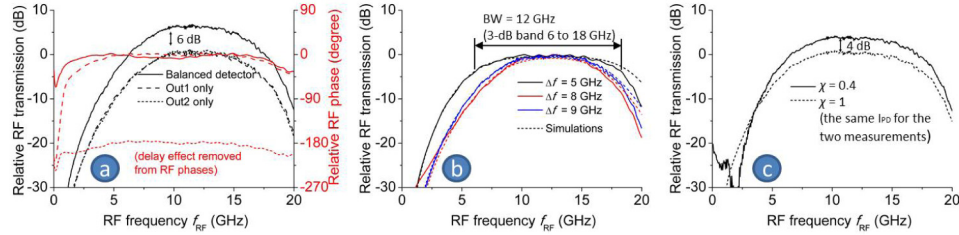
Fig. 9. (a) detected RF signals at the output of the balanced photodetector; (b) demonstration of RF bandwidth dependency on Δ*f* in comparison to the simulations; (c) demonstration of an extra RF gain achieved by performing carrier suppression technique.

4.2.3 PM-MPL performance

For the link performance measurement, the setup depicted in Fig. 7(b) was used and the PIC was configured as shown in Fig. 8(b) with $\Delta f_{Ch1} = \Delta f_{Ch2} = 5$ GHz. Similarly, a system calibration was first performed to eliminate the effects of the RF components connecting the PM-MPL and measurement equipment. In the realized non-amplified PM-MPL, the phase modulator has a $V_{\pi\text{-PM}} = 3.5$ V and a constant average photocurrent is maintained at $I_{DC} = 1$ mA. This low I_{DC} lies in a total optical loss of approximately 17 dB in the setup, where the PIC fiber-chip coupling loss amounts to 5 dB/facet (while 0.5 dB/facet is theoretically achievable when the optimized waveguide tapers are used [22]). Figure 10 depicts the measured two-tone (10 GHz ± 25 MHz) transmission of the link, where the results agree with the theoretical calculations and therefore prove the expected SFDR performance of the proposed PM-MPL. In principle, the residual spur of IMD2 in the output can be further reduced by optimizing the even-order cancellation of the balanced photodetector.
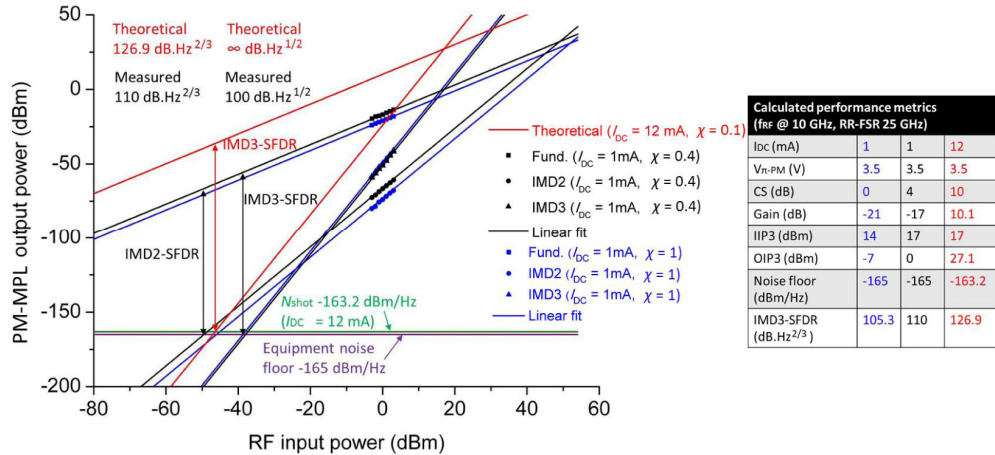

Fig. 10. Two-tone transmission measurements of the realized PM-PML with RF frequencies of 10 GHz ± 25 MHz for two different system parameter settings (black and blue), in comparison to a (red) theoretical calculation.

To verify the impact of the RRs on the system linearity, the RIP3$_{PM\text{-}RR}$ of the realized PM-MPL was measured for different RF frequencies. The results are depicted in Fig. 11(a), which agree with the theoretical calculations.

Furthermore, to investigate the impact of the proposed modulation transformer on the system noise. The system architecture in Fig. 3(a) was used with the RR configured to perform the modulation transformer functionality. In the setup, a CW laser with a RIN of −160 dB/Hz and a linewidth of 1MHz was employed (EM4-253-80-057), which gives rise to a significant conversion of laser phase noise to intensity noise for PM-MPLs using photonic

frequency discriminators [12]. The measured output noise versus the average photocurrent I_{DC} is depicted in Fig. 11(b). For this measurement, an erbium-doped fiber amplifier was used before the photodetector, which allows the optical intensity noise dominating in the output noise. It is exhibited that there is no significant change in the output noise when the modulation transformer PIC is replaced by an optical attenuator characterized by an equal device insertion loss. This result provides the prove that the RR-based modulation transformer allows nearly zero conversion of laser phase noise to intensity noise.
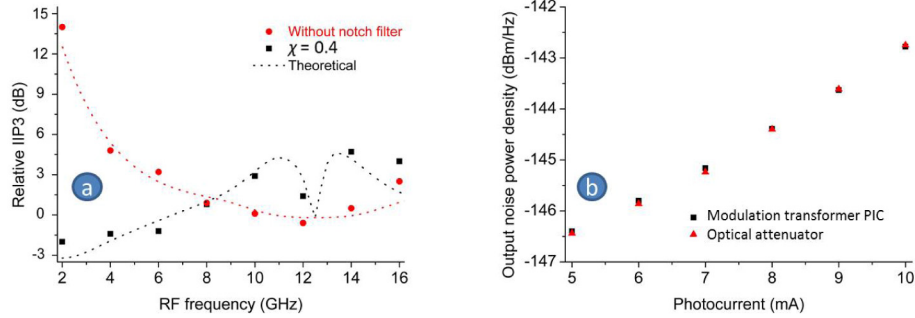
Fig. 11. (a) measured RIP3$_{PM-RR}$ of the realized PM-MPL for different RF frequencies; (b) optical intensity noise measurements regarding a RR-based modulation transformer and an optical attenuator with equal insertion loss. In the setup, a laser with a RIN of −160 dB/Hz and a linewidth of 1 MHz was employed, and an EDFA was used to boost the input optical power at the detector.

5. Conclusions

In this paper, a novel RR-based modulation transformer is proposed and experimental demonstrated, Using TriPleX^{TM} waveguide technology, a PIC consisting of two such modulation transformers and a notch filter has been fabricated, which is constructed using a 2×2 splitting circuit and 3 RRs with a free spectral range of 25 GHz. The device features simple architecture, stable operation, and easy reconfigurability. It is able to perform phase-to-intensity modulation transform and carrier suppression functionalities simultaneously. Based on the fabricated device, a PM-MPL has been realized, whose performance is comparable to that of a Class-AB MPL using low-biased MZMs. In agreement with the theory, the device demonstrates a 3-dB RF bandwidth of 12 GHz and allows nearly zero conversion of laser phase noise to intensity noise. In principle, the realized PM-MPL is free of IMD2. The IMD3-SFDR with $f_{RF} = 10$ GHz measures to be 110 dB.Hz$^{2/3}$ for the conditions $V_{\pi-PM} = 3.5$ V, $\chi = 0.4$, and $I_{DC} = 1$ mA. Potentially, this can be improved to 126.9 dB.Hz$^{2/3}$ if $\chi = 0.1$ and $I_{DC} = 12$ mA are provided instead. Moreover, the building block-based PIC design allows the proposed device to be integrated with more other functionalities on chip, which facilitates the creation of complex microwave photonic signal processors.

Appendix

Assume that $m_{RF1} = m_{RF2} = m$ and a small signal approximation where only $\Gamma_{p,q}$'s with frequencies $\leq 2f_{RF2}$ are considered for contributions in the photocurrent described in Eq. (8), then the amplitudes of the RF fundamental $|I_{1,0}|$ and IMD3 components $|I_{2,-1}|$, for example, can be described by

$$\left| I_{1,0}^{\text{Fund.}} \right|$$

$$= \left| A \cdot \text{Re} \{ \Gamma_{1,1} \Gamma_{0,1}^* + \Gamma_{2,0} \Gamma_{1,0}^* + \Gamma_{0,1} \Gamma_{-1,1}^* + \Gamma_{1,0} \Gamma_{0,0}^* + \Gamma_{0,0} \Gamma_{-1,0}^* + \Gamma_{1,-1} \Gamma_{0,-1}^* + \Gamma_{-1,0} \Gamma_{-2,0}^* + \Gamma_{0,-1} \Gamma_{-1,-1}^* \} \right|$$

$$= \left| A \right| \{ J_0(m) J_1(m)^3 \left| H_{RR}^{MT}(\nu_{RF1} + \nu_{RF2} - \Delta\nu) H_{RR}^{MT*}(\nu_{RF2} - \Delta\nu) H_{RR}^{NOF}(\nu_{RF1} + \nu_{RF2}) H_{RR}^{NOF*}(\nu_{RF2}) \right|$$

$$+ J_0^2(m) J_1(m) J_2(m) \left| H_{RR}^{MT}(2\nu_{RF1} - \Delta\nu) H_{RR}^{MT*}(\nu_{RF1} - \Delta\nu) H_{RR}^{NOF}(2\nu_{RF1}) H_{RR}^{NOF*}(\nu_{RF1}) \right|$$

$$- J_0(m) J_1^3(m) \left| H_{RR}^{MT}(\nu_{RF2} - \Delta\nu) H_{RR}^{MT*}(-\nu_{RF1} + \nu_{RF2} - \Delta\nu) H_{RR}^{NOF}(\nu_{RF2}) H_{RR}^{NOF*}(-\nu_{RF1} + \nu_{RF2}) \right|$$

$$+ J_0^3(m) J_1(m) \left| H_{RR}^{MT}(\nu_{RF1} - \Delta\nu) H_{RR}^{MT*}(-\Delta\nu) H_{RR}^{NOF}(\nu_{RF1}) H_{RR}^{NOF*}(0) \right|$$

$$- J_0^3(m) J_1(m) \left| H_{RR}^{MT}(-\Delta\nu) H_{RR}^{MT*}(-\nu_{RF1} - \Delta\nu) H_{RR}^{NOF}(0) H_{RR}^{NOF*}(-\nu_{RF1}) \right|$$

$$+ J_0(m) J_1^3(m) \left| H_{RR}^{MT}(\nu_{RF1} - \nu_{RF2} - \Delta\nu) H_{RR}^{MT*}(-\nu_{RF2} - \Delta\nu) H_{RR}^{NOF}(\nu_{RF1} - \nu_{RF2}) H_{RR}^{NOF*}(-\nu_{RF2}) \right|$$

$$- J_0^2(m) J_1(m) J_2(m) \left| H_{RR}^{MT}(-\nu_{RF1} - \Delta\nu) H_{RR}^{MT*}(-2\nu_{RF1} - \Delta\nu) H_{RR}^{NOF}(-\nu_{RF1}) H_{RR}^{NOF*}(-2\nu_{RF1}) \right|$$

$$- J_0(m) J_1^3(m) \left| H_{RR}^{MT}(-\nu_{RF2} - \Delta\nu) H_{RR}^{MT*}(-\nu_{RF1} - \nu_{RF2} - \Delta\nu) H_{RR}^{NOF}(-\nu_{RF2}) H_{RR}^{NOF*}(-\nu_{RF1} - \nu_{RF2}) \right| \}$$

$$(11)$$

$$\left| I_{2,-1}^{\text{IMD3}} \right|$$

$$= \left| A \cdot \text{Re} \{ \Gamma_{2,0} \Gamma_{0,2}^* + \Gamma_{2,-1} \Gamma_{0,0}^* + \Gamma_{1,0} \Gamma_{-1,1}^* + \Gamma_{1,-1} \Gamma_{-1,0}^* + \Gamma_{0,0} \Gamma_{-2,1}^* + \Gamma_{0,-1} \Gamma_{-2,0}^* \} \right|$$

$$= \left| A \right| \{ J_0^2(m) J_1(m) J_2(m) \left| H_{RR}^{MT}(2\nu_{RF1} - \Delta\nu) H_{RR}^{MT*}(\nu_{RF2} - \Delta\nu) H_{RR}^{NOF}(2\nu_{RF1}) H_{RR}^{NOF*}(\nu_{RF2}) \right|$$

$$- J_0^2(m) J_1(m) J_2(m) \left| H_{RR}^{MT}(2\nu_{RF1} - \nu_{RF2} - \Delta\nu) H_{RR}^{MT*}(-\Delta\nu) H_{RR}^{NOF}(2\nu_{RF1} - \nu_{RF2}) H_{RR}^{NOF*}(0) \right|$$

$$- J_0(m) J_1^3(m) \left| H_{RR}^{MT}(\nu_{RF1} - \Delta\nu) H_{RR}^{MT*}(-\nu_{RF1} + \nu_{RF2} - \Delta\nu) H_{RR}^{NOF}(\nu_{RF1}) H_{RR}^{NOF*}(-\nu_{RF1} + \nu_{RF2}) \right|$$

$$+ J_0(m) J_1^3(m) \left| H_{RR}^{MT}(\nu_{RF1} - \nu_{RF2} - \Delta\nu) H_{RR}^{MT*}(-\nu_{RF1} - \Delta\nu) H_{RR}^{NOF}(\nu_{RF1} - \nu_{RF2}) H_{RR}^{NOF*}(-\nu_{RF1}) \right|$$

$$+ J_0^2(m) J_1(m) J_2(m) \left| H_{RR}^{MT}(-\Delta\nu) H_{RR}^{MT*}(-2\nu_{RF1} + \nu_{RF2} - \Delta\nu) H_{RR}^{NOF}(0) H_{RR}^{NOF*}(-2\nu_{RF1} + \nu_{RF2}) \right|$$

$$- J_0^2(m) J_1(m) J_2(m) \left| H_{RR}^{MT}(-\nu_{RF2} - \Delta\nu) H_{RR}^{MT*}(-2\nu_{RF1} - \Delta\nu) H_{RR}^{NOF}(-\nu_{RF2}) H_{RR}^{NOF*}(-2\nu_{RF1}) \right| \}$$

$$(12)$$

The corresponding OIP3 and the IMD3-SFDR (impedance-matched case) can be given by

$$\text{OIP3} = \frac{R_L}{2} I_{1,0}^{\text{Fund.}}(m)^2 \quad \text{for} \quad \left| I_{1,0}^{\text{Fund.}}(m) \right| = \left| I_{2,-1}^{\text{IMD3}}(m) \right| \tag{13}$$

$$\text{SFDR} = 2/3(\text{OIP3}_{\text{dBm}} - S_{\text{th}} - 1/4(S_{\text{shot}} + S_{\text{RIN}})) \tag{14}$$

Acknowledgment